A case study investigation into the effects of spatially dependent convection coefficients on the fatigue response of a power plant header component

J. P. Rouse[1], P. Zacharzewski[1], C. J. Hyde[1], R. Jefferson-Loveday[1], A. Morris[2] and S. T. Kyaw[3]

[1]Gas Turbine and Transmissions Research Centre (G2TRC), University of Nottingham, NG7 2TU, UK
[2]EDF Energy, West Burton Power Station, Retford, Nottinghamshire, DN22 9BL, UK
[3]Department of Mechanical, Materials and Design Engineering, Sheffield Hallam University, City Campus, Howard Street, Sheffield, S1 1WB, UK

Abstract: Societal and environmental pressures are forcing thermal power plant operators to deviate greatly from the generation strategies of the past. The application of high frequency start up/shut down/partial load cycles to components that may well be outside their design life makes research into the long-term integrity of at risk assets paramount. Decoupled thermal/mechanical analyses have been used in the literature to estimate anisothermal fatigue in header components, with convective boundary conditions typically assumed for internal surfaces in order to determine heat fluxes and hence a temperature field. In reality, convective coefficients are heavily dependent upon local velocity profiles. In the present work, computational fluid dynamics is used in order to better approximate the steam flow in a real power plant header, leading to a convection coefficient field that is used to solve the thermal problem. Anisothermal fatigue analysis is finally conducted using a Chaboche type model. The results of computational fluid dynamics have illustrated that heat transfer coefficient values can vary (spatially) by a factor of 5.49 over the internal header wall, with noticeable hot spots in the wake of the stub penetrations. Peak differences of 6.47% in accumulated plastic strain levels have been observed between simulations conducted with constant (simplified) and variable (computational fluid dynamics derived) thermal boundary conditions.
Keywords: *Heat Transfer Coefficient, Power Plant, Header, Cyclic-Plasticity, Computational Fluid Dynamics*

1 Introduction

Thermal power plants are increasingly expected to generate according to "two-shifting"[1] operating strategies, whereby plant is kept warm at partial load so that it may be brought up to full load quickly if electricity unit prices warrant it. Such trends are a reaction to a paradigm shift in how electricity is generated. Renewable sources are more frequently relied upon to provide baseline load while ageing thermal plant ensures that energy demands are met. With the introduction of new legislation regarding the burning of fossil fuels and strict carbon tariffs, this generation strategy is one of the few ways that large coal plants can make a profit. The UK has many large fossil fuel power stations that were commissioned in the 1960's/70's and these plants were not designed to operate under high frequency start up/partial load/shut down conditions. There are therefore legitimate concerns in industry over the long term strucutral integrity of certain components in the steam path. During fast ramp up periods potentially significant thermal stresses can develop in thick walled components, leading to the accumulation of plastic strain and premature failure. Similar concerns exist in other parts of the world, where mothballed or ageing plant is now being driven in an aggressive manner in order to compete with renewable energy. Alternatively, in the developing world, new thermal plant is being commissioned and it is expected that in the near future these contemporary plants will face the same challenges. In short, there is an understandable concern in the power industry over the medium-long term strucutral integrity of certain components due to a radical change in generation practices.

Headers have been identified as an "at risk" component by industry (the replacement of a failed component can cost £1.5-2M) and have therefore received attention in the literature. The analysis of a header during an operation cycle is commonly achieved using un-coupled thermo-mechanical analyses, wherein a temperature field is found in a primary simulation by applying thermal boundary conditions and solving the heat equation. These time dependent temperature fields are then used in secondary mechanical analyses (thereby

allowing thermal expansion and temperature dependent material parameters to be accounted for)[2,3]. Clearly, this approach makes several important assumptions regarding the interplay between thermodynamic quantities. Such a decoupled approach cannot account for dissipation of plastic work as heat during loading, however the present work is concerned with a far more basic assumption. Commonly, heat transfer coefficients used in the thermal analyses are assumed to be constant (either over the entire model or in specific regions where fluid velocities are judged to be approximately uniform). In reality, local heat transfer coefficients will depend on the exact flow profile however.

Computational fluid dynamics (CFD) is utilised in the present work to determine local heat transfer coefficients at the wall of a superheater outlet header. Flow boundary conditions have been idealised (more detail of this can be found section 2) for a "unit cell" of the header geometry (i.e circulation through the shell is neglected, see figure 1). A P91 (CMV) steel is used here as an example material (for the thermal and mechanical analyses). P91 has been referred to as "the work horse of the power industry" and is widely deployed in numerous plants. Header dimensions used here are typical of P91 examples, with a shell external diameter and wall thickness of $420mm$ and $89mm$, respectively and s stub penetration external diameter and wall thickness of $57mm$ and $12.5mm$, respectively.

A full load component mass flow rate of $29.31kg/s$ has been applied in CFD analyses; this value is based on the rate maximum flow rate for an in service turbine and is in agreement with published values[4]. In order to satisfy continuity, the component mass flow rate is assumed to be distributed equally between all stub penetrations (84 in the present case), resulting in an inlet mass flow rate of $0.349kg/s$ (through stub penetrations). Both full load and half load conditions have been modelled using CFD in order to demonstrate the range of heat transfer coefficients that may be encountered during two shifting, with the latter simply half of the full load mass flow condition.

A particular driver in this research (from an industry perspective) is to improve the understanding of how different start up requirements (i.e. the time required to come on to full generation load) affect component integrity. To investigate this here, a generalised load profile (this can be thought of as the source steam temperature and internal pressure time profiles which are applied in finite element analysis, FEA, simulations) has been generated from Fourier series analysis of real plant transient data (see figure 2, where T is steam temperature and T_M is the maximum steam temperature, $843K$). Time periods during "at load" and "shut down" conditions are given in figure 2 and are common over all FEA simulations. The hot start time (t_{start} in figure 2, the time for steam temperatures to reach T_M from the partial load starting temperature, here $693K$) however has been varied between analyses, with profiles using values of $2.5hrs$ (a fast start under present conditions), $0.5hrs$ (a suggested fast start limit based on UK trials[5]) and $0.25hrs$ (a very fast start used for illustrative purposes in the present work). High internal pressures are applied to the header component here ($396.8bar$; approximately 2.5 times greater than those typically used in pulverised coal plants in the UK). This has been done to exaggerate plastic strain accumulation during mechanical FEA and is judged to be reasonable as the aim of the present study is to assess the effects of thermal boundary conditions in header component analyses. It must however be noted that plastic strain accumulation rates reported here are not truly representative of real world conditions.

It is a feature of many elastic visco-plastic models which attempt to approximate the cyclic behaviour of materials such as P91 that values for the (initial) size of the yield locus (or, perhaps more aptly, the equal dissipation surface in the viscous case) are low in magnitude when compared to the results derived from monotonic experimentation. Such effects are discussed in the work of Barrett et al.[6] and Rouse et al.[7], and are particularly noted when high temperature experimental data is used for material parameter optimisation. In visco-plastic material model formulations viscous stress will saturate to the instantaneous size of the yield locus. If visco-elastic effects are neglected, long term stress relaxation during, say, periods of strain hold can only be accurately replicated by reducing the magnitude of the initial yield stress (k in the present work, see section 3.1). The physical significance of k has been preserved in the present work however by setting boundaries in the material parameter optimisation procedure which are informed by monotonic results. In component simulations which use realistic internal steam pressures however, these representative values of yield stress only allow for a response which is almost entirely elastic to be predicted. Such effects are not representative of real world components, as damage (loss of load carrying capability) can still be caused at relatively modest stress levels by visco-elastic phenomenon. Future work will look to include visco-elastic effects (see section 4), however in lieu of suitable predictive models the present work uses high levels of internal pressure to create a âĂIJbaselineâĂİ stress field about which thermally induced stresses (resulting from either constant or spatially dependent heat transfer coefficients) can fluctuate, and thereby inducing plasticity and a viscous response.

Readers should note that, in the present analyses, single material component models are assumed. That is to say, there is no incorporation of material variations due to the presence of weldments in the model (however a fillet is included at the stub penetrations that is similar to the weld toe, see figure 1). Weldments have been recognised for some time are important regions of local geometric/material discontinuity which have the potential to act as failure initialisation location (for example, type IV cracking in HAZ regions due to creep has been investigated by Saber et al.[8]). Inter-ligament cracking between stub penetrations has also been identified in the literature for headers (see Viswanathan[9,10]) and industrial experience has indicated that this is a result of high frequency start up/shut down/partial load operating practices ("two shifting"). As the present work is focused on the effects of

heat transfer on stress analysis in header components and computational fluid dynamics (CFD) has revealed that heat transfer coefficients in this region are comparatively uniform, it is judged to be reasonable that weld regions are neglected from the presented component models. It should also be noted the discontinuities around weldments are typically highly localised, suggesting that the inclusion of local stiffness variations (due to the presence of a weld) are unlikely to cause significant alternations to the stress fields at the points of interests discussed below in section 3.5.

This idealisation is judged to be reasonable as previous experience has suggested that peak stress/plastic strain accumulation points do not occur at the welds (see section 3.5) and it is expected that weld sections will not significantly affect the global stiffness of the component model.

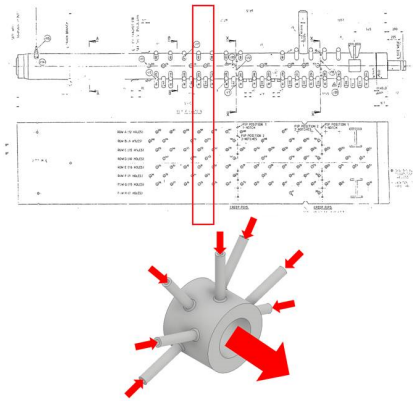

Figure 1: An overview of the superheater outlet header model "unit cell" used in the present work, with assumed flow directions/sources indicated.

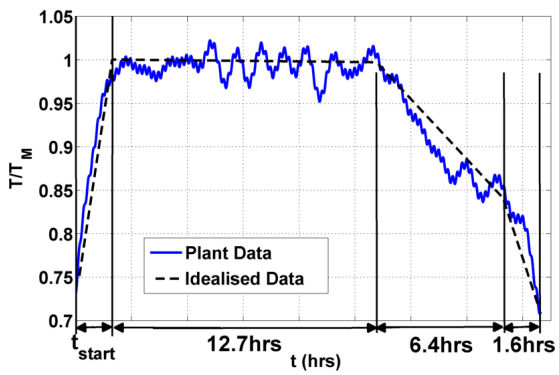

Figure 2: The generalised start up waveform.

2 CFD Analysis of a Header Component

2.1 Model Development and Boundary Conditions

CFD simulations of the header component have been completed in ANSYS' Fluent software using a standard incompressible SIMPLE scheme with a k-omega closure shear stress transportation (SST, based on the work of Menter[11]) turbulence model. An overview of the developed CFD model can be seen in figure 3; note that flow is assumed to propagate along the x axis (see figure 1), with mass flow inlet conditions defined at each stub penetration and Neumann outlet conditions given at the upstream shell bore.

Initial simulations used only a single unit cell of the geometry and suggested highly turbulent flow patterns with difficulties in solution convergence. Second order accuracy unsteady Reynold's averaged Navier-Stokes (URANS) simulations were therefore conducted, wherein two flow development unit cells were placed upstream of the control region (see figure 3). In the final simulations, 2 flow through simulations (with a step time of $5 \times 10^{-5} s$) were initially performed in order to develop the flow, with results in the control region averaged over the subsequent 3 flow through simulations. Heat transfer coefficients in the model were determined using equation (1), where T_{hot} and T_{cold} (representing the inflow and wall temperatures, respectively) were assumed to be $841K$ and $820K$, respectively, and $\dot{q}$ is the calculated wall heat flux. Assumed flow medium parameters are given in table 1. An example contour plot of surface heat transfer coefficients is presented in figure 4. Note that the results used in the remainder of the work are taken from the third set of stub penetrations (i.e. those furthest to the right in figure 4).

Readers should note that, at present, only a single set of steam conditions are considered for the calculation of heat transfer coefficient fields by CFD (see table 1). These conditions are representative of steam at full load in a coal fired sub-critical, namely $841K$ and $166bar$. The single steam condition was chosen in order top replicate the steam flow pattern at the point in operation when the header material experiences particularly arduous conditions (i.e. high temperature, implying relatively yielding conditions and significant viscous effects). A more detailed analysis of the effects of assumed steam condition on heat transfer coefficient field can be found below in section 4.

$$h = \frac{\dot{q}}{T_{hot} - T_{cold}} \tag{1}$$

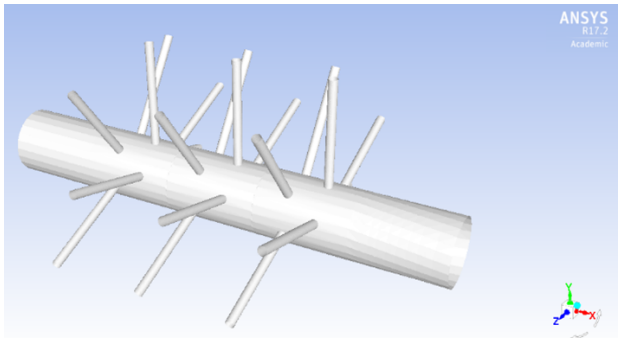

Figure 3: Fluent header model, showing upstream flow profile development regions.

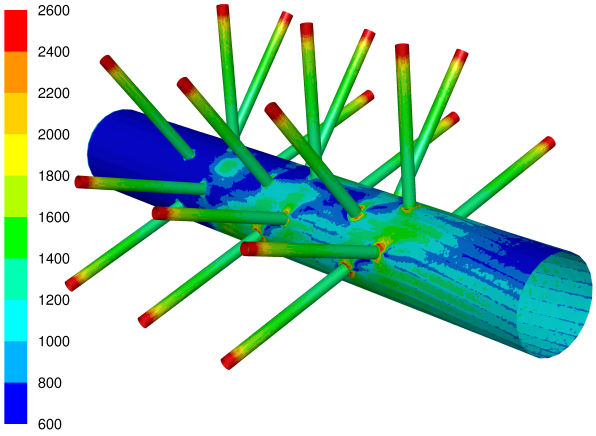

Figure 4: An example heat transfer coefficient surface contour plot for the Fluent header model shown in figure 3 (under full load conditions).

Table 1: Assumed steam flow properties used in CFD simulations (representative of steam at $841K$ and $166bar$)[12].

Density ($\rho, kg/m^3$)	47.6
Specific Heat Capacity ($C_P, kJ/kg.K$)	1.912
Thermal Conductivity ($k, W/m.K$)	0.09009983
Dynamic Viscosity ($\nu, kg/m.s$)	$3.22915x10^{-5}$
Operating Pressure (Gauge, bar)	166
Specific Heat Ratio (C_P/C_V)	1.4

2.2 Results

As discussed in section 1, two loading conditions have been considered in the present work; namely a full load and half load case. Mass flow rates of $0.349kg/s$ and $0.174kg/s$ were applied to inlet stub penetrations, respectively. For the full load conditions, approximate Reynold's number values of 38000 and 320000 were found for the stub and shell sections, respectively. Local heat transfer coefficient values at nodal positions on the component internal wall (for the shell section) are plotted in figures 5 and 6 for the full and half load conditions, respectively. Note that a $\theta = 0$ plane has been defined using the XY plane in figure 3 (using the negative Y half-plane to define 0). Heat transfer coefficient fields can be seen to be approximately symmetric about the $\theta = \pi$ plane; this observation has been used in thermal and mechanical FEA simulations to impose a similar plane of symmetry (see section 3.5). CFD results revealed that heat transfer coefficients where approximately constant for stub penetration sections, therefore these regions have been modelled using uniform heat transfer coefficient values in all analyses ($1401.1W/m^2.K$ and $886.53W/m^2.K$ for the full and half load cases, respectively). Uniform heat transfer coefficient fields are applied to the header shell sections for all loading cases (in addition to applying varying heat transfer coefficient fields based on CFD results) in thermal FEA simulations (these are referred to as "HTC Constant" analyses is section 3.5). Uniform shell heat transfer coefficient values were determined by averaging the CFD determined heat transfer coefficient field over the unit cell shell area. These were determined to be $1219.4W/m^2.K$ and $697.16W/m^2.K$ for the full load and half load conditions, respectively.

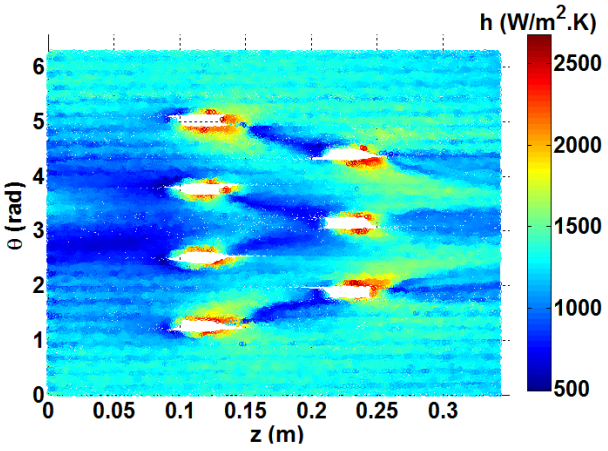

Figure 5: Full load condition CFD based heat transfer coefficient field for the header internal shell surface.

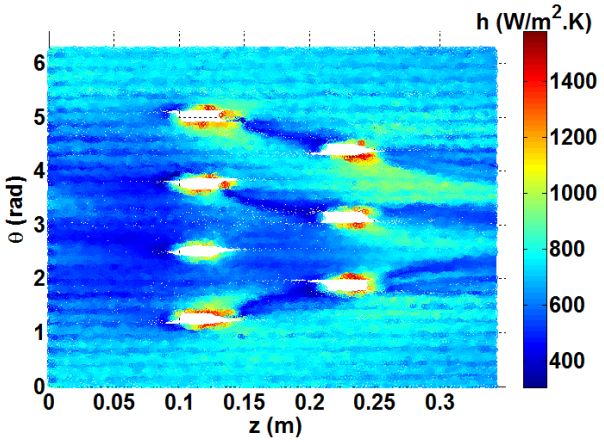

Figure 6: Half load condition CFD based heat transfer coefficient field for the header internal shell surface.

3 Anisothermal Cyclic Plasticity Analysis of a Header Component

3.1 Visco-Plastic Material Model

A Chaboche type[13,14] visco-plastic material model is applied in the present work, with temperature dependent modifications applied to the isotropic and kinematic hardening components (see the work of Barrett et al[6]). A brief overview is given here, however a complete discussion of the assumed material model and the material constant determination procedures can be found in the work of Kyaw et al[15].

Total strain (ε_T) is decomposed into elastic, plastic and thermal components ($\boldsymbol{\varepsilon}_T = \boldsymbol{\varepsilon}_e + \boldsymbol{\varepsilon}_p + \boldsymbol{\varepsilon}_{th}$, respectively). Non-linear kinematic hardening is expressed through the use of several differential equations that update the relevant kinematic variables. In this way, only one surface definition is required (the yielding surface). For the Chaboche model, the yield function is defined by equation (2).

$$f = J\left(\boldsymbol{\sigma} - \boldsymbol{\chi}\right) - R - k \tag{2}$$

where the back stress tensor ($\boldsymbol{\chi}$) designates the centre of a "yield" surface and the drag stress (R) denotes the variation of its size (this can either act to increase or decrease the size of the yield surface). Through the use of these quantities, kinematic and isotropic hardening may be represented, respectively. Readers should note that the term yield surface is used here in order to convey the function of the visco-plastic model to those who may not be immediately familiar with it. The surface described by equation (2) may more appropriately be described as a surface of equal dissipation. In the time independent elastic-plastic case $f <= 0$ at all times. When viscous effects are considered however f may take a value greater than 0 (note that, during stress relaxation, this value will reduce with time until $f = 0$). The function $J\left(\boldsymbol{\sigma} - \boldsymbol{\chi}\right)$ allows for the interpretation of a distance in stress space (the scalar equivalent in the deviatoric space[16]), which for a von Mises material can be characterised by equation (3).

$$J\left(\boldsymbol{\sigma} - \boldsymbol{\chi}\right) = \left[\frac{3}{2}\left(\boldsymbol{S} - \acute{\boldsymbol{\chi}}\right)\left(\boldsymbol{S} - \acute{\boldsymbol{\chi}}\right)\right]^{1/2} \tag{3}$$

where $\boldsymbol{S}$ and $\acute{\boldsymbol{\chi}}$ are the deviatoric tensors forms of $\boldsymbol{\sigma}$ (the stress tensor) and $\boldsymbol{\chi}$ (the back stress tensor), respectively. Increments for the stress tensor ($\Delta\boldsymbol{\sigma}$) may be calculated using Hooke's law[17,18] (see equation (4)) , where the "mechanical" strain increment is defined as $\Delta\boldsymbol{\varepsilon}_M = \Delta\boldsymbol{\varepsilon}_T - \Delta\boldsymbol{\varepsilon}_{th}$ λ & μ are the Lamé constants, α is the coefficient of thermal expansion, $\boldsymbol{I}$ is the identity matrix, and ΔT is the instantaneous temperature increment. The thermal strain increment ($\Delta\boldsymbol{\varepsilon}_{th}$) may be defined by equation (5).

$$\Delta\boldsymbol{\sigma} = \lambda Tr\left(\Delta\boldsymbol{\varepsilon}_M - \Delta\boldsymbol{\varepsilon}_p\right) + 2\mu\left(\Delta\boldsymbol{\varepsilon}_M - \Delta\boldsymbol{\varepsilon}_p\right) - \left(3\lambda + 2\mu\right)\Delta T\boldsymbol{I} \tag{4}$$

$$\Delta\boldsymbol{\varepsilon}_{th} = \alpha\Delta T\boldsymbol{I} \tag{5}$$

To provide a better approximation of the kinematic effects the back stress can be decomposed into several components (by way of example, two back stress components will be used here). An Armstrong and Frederick type kinematic hardening law can be used to define the increment for each component, taking the form of equation (6). It is noted that in equation (6) temperature rate dependency in the hardening modulus term (C_i) only is accounted for (i.e. temperature rate dependency in the dynamic recovery term is neglected). Several physical/phenomenological/thermodynamic justifications for this are given in Chaboche's review of viscoplasticity[19]. These may be briefly summarised as 1). rapid changes in temperature yield a change in modulus that instantaneously alters the internal stress field associated with plastic incompatibilities and 2). the last term in equation (6) directly follows from assuming a quadratic form (using the back strain tensor as the independent state variable) of the plastic component of the Helmholtz free energy (the energy stored in the material by kinematic hardening).

$$\dot{\boldsymbol{\chi}}_i = \frac{2}{3}C_i\dot{\boldsymbol{\varepsilon}_p} - \gamma_i\boldsymbol{\chi}_i\dot{p} + \frac{1}{C_i}\frac{\delta C_i}{\delta T}\boldsymbol{\chi}_i\dot{T} \tag{6}$$

where C_i and γ_i are temperature dependent material constants (C_i defines the stationary value and γ_i dictates how quickly this value is achieved[20,21]). The accumulated plastic strain (p) is a monotonic quantity and is the summation of the modulus of the plastic strain values (equation (7)). Note that T is the instantaneous particle temperature.

$$dp = \left|d\boldsymbol{\varepsilon}_{\boldsymbol{p}}\right| \tag{7}$$

By decomposing the back stress into multiple components, transient and long term behaviour may be accounted for, here with γ_1 and C_1 describing initial non-linearity and γ_2 and C_2 describing asymptotic behaviour. The total back stress is

given as a summation of these components, therefore for N components, the total back stress ($\boldsymbol{\chi}$) is given by equation (8).

$$\boldsymbol{\chi} = \sum_{i=1}^{N} \boldsymbol{\chi}_i \tag{8}$$

Variations in the scalar drag stress (R) will represent the effects of isotropic hardening and, as such, will alter only the size of the yield surface. In the form originally presented by Chaboche, only primary behaviour (either hardening or softening) is represented. The drag stress will undergo some initial monotonic increment before reaching a stabilised asymptotic value. This saturated value is signified by Q, with the rate at which this stabilised value is reached being determined by b, see equation (9). Long term linear isotropic softening in equation (9) is accounted for through the parameter H. Note that temperature dependencies in Q, b and H are considered in equation (9) (see the work of Zhang et al[22]), where the quantity r_2 is expressed by equation (10).

$$\dot{R} = bQ\dot{r}_2 + r_2\left(\frac{\delta b}{\delta T}Q + \frac{\delta Q}{\delta T b}\right)\dot{T} + H\dot{p} + \frac{\delta H}{\delta T}p\dot{T} \tag{9}$$

$$r_2 = \frac{1}{b}\left(1 - e^{-bp}\right) \tag{10}$$

Viscous effects will be present when time or strain rate has an influence on inelastic behaviour[23]. Time dependent behaviour can be introduced through the definition of a viscous stress (σ_v), forming a component of total stress, summarised in equation (11).

$$\boldsymbol{\sigma} = \boldsymbol{\chi} + \left[(R + k + \sigma_v)\, sgn\left(\boldsymbol{\sigma} - \boldsymbol{\chi}\right)\right]\boldsymbol{n} \tag{11}$$

where the function $sgn(x)$ is specified by equation (12).

$$sgn(x) = \begin{cases} 1 & \text{if } x > 0 \\ 0 & \text{if } x = 0 \\ -1 & \text{if } x < 0 \end{cases} \tag{12}$$

Note that, in equation (11), the quantity $\boldsymbol{n}$ is defined as the direction of plastic strain rate and may be expressed by equation (13).

$$\boldsymbol{n} = \frac{3}{2}\frac{\boldsymbol{S} - \acute{\boldsymbol{\chi}}}{J\left(\boldsymbol{\sigma} - \boldsymbol{\chi}\right)} \tag{13}$$

The viscous stress takes the form of a power law, see equation (14), where Z and n are viscous material coefficients.

$$\sigma_v = Z\dot{p}^{1/n} \tag{14}$$

To find the plastic strain increment ($d\boldsymbol{\varepsilon_p}$) the flow rule with a normality condition is applied. To find the normal direction, the yield surface translation vector ($\boldsymbol{S} - \acute{\boldsymbol{\chi}}$) is normalised to produce a unit vector. The size of the yield surface is given by $R + k$, however for the limiting condition of yield surface (when $f = 0$), shown in equation (15) is also true.

$$J\left(\boldsymbol{\sigma} - \boldsymbol{\chi}\right) = R + k \tag{15}$$

The flow rule can therefore be written as equation (16)[23].

$$\frac{d\boldsymbol{\varepsilon_p}}{dt} = \frac{3}{2}d\lambda\frac{\boldsymbol{S} - \acute{\boldsymbol{\chi}}}{J\left(\boldsymbol{\sigma} - \boldsymbol{\chi}\right)} \tag{16}$$

where $d\lambda$ is the plastic multiplier, which is given by equation (17). The plastic strain increment ($d\boldsymbol{\varepsilon_p}$) may therefore be calculated from equation (18).

$$d\lambda = \left[\frac{\langle f \rangle}{Z}\right]^n \tag{17}$$

$$d\varepsilon_p = \frac{3}{2}\left\langle\frac{J\left(\boldsymbol{\sigma} - \boldsymbol{\chi}\right) - R - k}{Z}\right\rangle^n \frac{\boldsymbol{S} - \acute{\boldsymbol{\chi}}}{J\left(\boldsymbol{\sigma} - \boldsymbol{\chi}\right)}dt \tag{18}$$

Note that the definition of the brackets used in equation (18) is given in equation (19).

$$\langle x \rangle = \begin{cases} x & \text{if } x \geq 0 \\ 0 & \text{if } x < 0 \end{cases} \tag{19}$$

Multi-axial implementation of the material model described above is achieved using the UMAT capability within the commercial finite element package ABAQUS[24]. More specifically, the implicit scheme described in the work of Dunne and Petrinic[25] is implemented, wherein increments p are estimated for a time step using an iterative approach (with a starting point based on a purely elastic-plastic approximation). Increments in all other dual variables can be derived as a result of approximating the increment in p.

3.2 Isothermal Material Parameter Determination and Experimental Methods

The viscoplastic model described in section 3.1 uses a total of 11 temperature and material dependent parameters (for isotropic materials) that must be defined before it can be applied. Additionally, rates of change of the parameters C_1, C_2, b, Q, and H with respect to temperature must be defined for an-isothermal loading conditions. A brief discussion of the material parameter optimisation procedure implemented in the present work is given here, however more detail (particularly with reference to the use of Cottrell's stress partitioning method[26,27]) can be found in the authors' previous work[7,15].

All experimental data was collected using an Instron 8862 testing rig that utilises radio frequency induction heating. Temperature was controlled using Type K thermocouples, controlling to the shoulder of the gauge section in isothermal cases and the centre of the gauge section in anisothermal experiments (unacceptable levels of lag were observed when controlling to the shoulder for dynamic loading sequences). Prior to testing, calibration samples (with a distribution of thermocouples over the gauge section) were used to check

temperature uniformity (in accordance with ISO/TC 164/SC5) for a given coil design. In all cases, loading waveforms were fully reversed ($R = -1$) and strain controlled (using a spring-loaded extensometer). $6.5mm$ gauge section diameter solid samples were used in isothermal tests, with anisothermal tests performed using hollow samples of identical external diameter. The use of hollow samples allowed cooling air supplies to be injected along the centreline, thereby improving the control of temperature rates and ensuring that they could be matched to mechanical loading rates. This is turn allowed for the use of in phase (IP) and out of phase (OP) an-isothermal loading patterns. In isothermal tests, both "sawtooth" (standard triangular) and "dwell" type (wherein $120s$ strain hold periods were applied at the end of tensile loading branches) strain load waveforms were applied to the samples. It is worth noting here that the hold periods used in the presented experimental program are short when compared to the hold periods experienced by in service power plant components. It is well known that the power law viscous stress formulation presented above is capable of describing viscous effects within a narrow range of loading rates only, suggesting that trying to optimise the model against extended data sets will yield significant deviations from realistic behaviour over the entire loading rate range. $120s$ dwell periods have been shown in the authors' previous work to be sufficient for developing models that predict a good level of viscous response for P91[7]. Possible future extensions that address this deficiency are the inclusion of a hyperbolic sine based flow rule or the incorporation of additional viscous mechanisms in the model formulation. Both of these would allow for additional stress relation data to be considered. In an-isothermal testing only "sawtooth" waveforms were applied (with corresponding temperature waveforms). A strain rate of $0.1\%/s$ was used for all tests (with corresponding temperature rates applied where applicable) and strain limits were set to $\pm 0.5\%$. Test temperatures/temperature limits (in the case of an-isothermal testing) were set to 600^oC, 500^oC, and 400^oC (these values were chosen as they are representative two-shifting power plant steam temperatures for sub-critical plant).

Material constant optimisation was conducted against isothermal experimental data only using a bespoke MATLAB program that referenced all available experimental data for a particular test temperature simultaneously (that is to say, series optimisation was implemented[7]). The uniaxial (and isothermal) formulation of the material model was solved using ODE45 (a Dormand-Prince pair $4^{th}/5^{th}$ order explicit Runge-Kutta method), with non-linear least squares optimisation controlled using LSQNONLIN (the Levenburg-Marquadt algorithm)[28,29]. A single objective function was used to compare stresses (experimental and predicted, σ_{ij}^{exp} and σ_{ij}^{pred} respectively) at defined sample points, see equation (20) (where N_{cycle} is the number of loading cycles under consideration and N_{sample} is the number of sampling points). In the present work, $N_{sample} = 20$ and $N_{cycle} = 400$ for all cases.

$$F(\boldsymbol{x}) = \sum_{i=1}^{N_{cycle}} \sum_{j=1}^{N_{sample}} \left(\sigma_{ij}^{exp}\right)^2 - \left(\sigma_{ij}^{pred}\right)^2 \qquad (20)$$

Initial estimates of the temperature dependent material parameters have been determined by the Cottrell stress partitioning method, wherein the yield locus is defined for each experimental hysteresis loop by searching for yield points in the tensile and compressive loading branches (see Kyaw et al. for more details on this procedure[15]). With the yield locus identified, estimates of the evolution of χ and R with respect to plastic strain may be made and approximate versions of equations (6) and (9) fitted (thereby yielding estimates of the 11 material parameters). Upper and lower bounds (UB and LB, respectively) were defined in the optimisation procedure based on these initial estimates (see table 2).

Table 2: A summary of lower (LB) and upper (UB) bounds used in isothermal material constant optimisation.

Constant	LB	UB
γ_1	0	$\gamma_1^0 + \gamma_2^0$
C_1	0	$100 \max\left(C_1^0, C_2^0\right)$
γ_2	0	$\gamma_1^0 + \gamma_2^0$
C_2	0	$100 \max\left(C_1^0, C_2^0\right)$
Z	0	$100Z^0$
n	$0.5n^0$	$1.5n^0$
b	$0.5b^0$	$1.5b^0$
Q	$1.2Q^0$	$0.8Q^0$
k	$k^0 - 25$	$k^0 + 25$
E	$E^0/100$	$100E^0$
H	$1.5H^0$	$0.5H^0$

As described above, optimisation procedures were separated on a test temperature basis (i.e. separate sets of constants were determined for 600^oC, 500^oC, and 400^oC conditions) using isothermal experimental data only. Linear relationships were then fitted to each material parameter in order to establish a set temperature dependent function which may be easily implemented in the equations in section 3.1 (temperature dependent derivative are after all now constants, being equal to the gradient of the linear parameter fits). Parameter functions are given in equation (21), with plots showing the relationship between optimised parameter value and functional approximation are given in figure 7 (note that for presentational reasons parameter values have been normalised against the corresponding maximum optimised value and values of T in equation (21) are given in °C). Readers should note that linear fits have been applied in the present work out of convenience (derivatives with respect to temperature are of course constants in this case), however remarkable correlations can be observed for elastic, viscous, and isotropic material parameters (see figure 7 b). and c).). Kinematic parameters (notably C_1 and C_2 in figure 7 a).) are less accurately predicted, with peak differences of approximately 30% observed when comparing the results of optimisation to the linear temperature dependent approximation. A loss of fidelity is judged to be

permissible in the present work as values for γ_1 and γ_2 are well predicted using the linear fits, indicating that saturation of the kinematic components (which is typically fast in P91) can be appropriately represented. This sentiment is borne out in section 3.3, where an excellent level of agreement is acheived between experimental data and predictions made using the functions shown in equation (21).

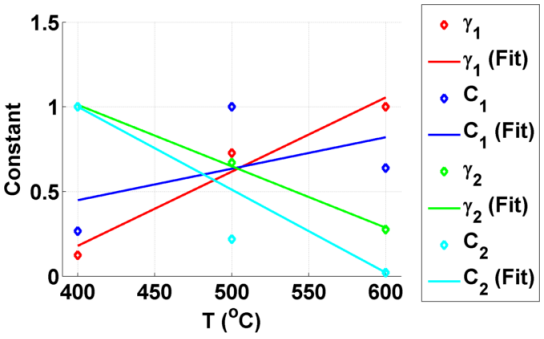

(a)

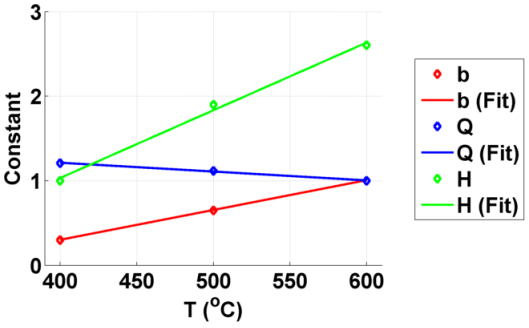

(b)

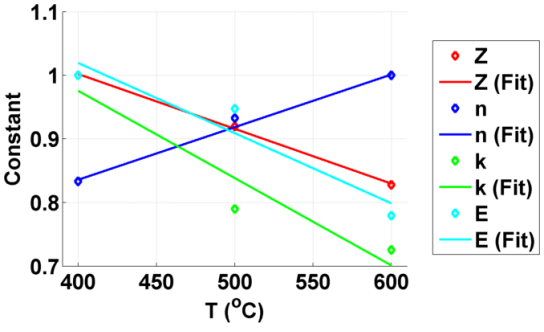

(c)

Figure 7: Plots of normalised (against peak optimised value in the $400-600^oC$ range) constant values, showing (a) kinematic, (b) isotropic, and (c) viscous/elastic related constants. In all cases, constants resulting from optimisation (on isothermal data) are marked by diamond points. Linear fits (given in equation (21)) are also plotted for reference.

$$
\begin{aligned}
\gamma_1 &= 2.5449T - 913.59 \\
C_1(MPa) &= 62.047T - 9805.6 \\
\gamma_2 &= -3.7521T + 2547.2 \\
C_2(MPa) &= -707.95T + 427833 \\
Z(MPa.s^{1/n}) &= -2.6524T + 4146.2 \\
n &= 0.0018T + 1.099 \\
b &= 0.0071T - 2.2322 \\
Q(MPa) &= 0.0458T - 71.447 \\
k(MPa) &= -0.2818T + 313.08 \\
E(GPa) &= -0.188T + 248.85 \\
H(MPa) &= -0.0125T + 3.3847
\end{aligned}
\tag{21}
$$

Instantaneous coefficients of thermal expansion, α, were determined previously for the P91 material using a TA instruments Q400 thermomechanical analyser[3] (see table 3).

Table 3: Temperature-dependent thermal expansion coefficients (representative of a P91 chromium steel), determined through experimental data fitting, used in the FEA modelling.

T (°C)	400	500	600
α (K^{-1})	1.340^{-5}	1.380^{-5}	1.420^{-5}

3.3 Isothermal and Anisothermal Model Predictive Capability (Uniaxial Validation)

Isothermal and anisothermal cyclic behaviour has been predicted using the model described in the previous section, with results compared to experimental investigations. This was done to 1). determine temperature dependent material properties through an optimisation routine (using isothermal results) and 2). validate the identified material constant functions (using anisothermal results). Predictions of material response are presented here in figures 8 to 13 for isothermal loading conditions (600^oC, 500^oC, and 400^oC) under "dwell" and "sawtooth" loading waveforms, respectively. In all cases, predictions of the 1^{st}, 200^{th}, and 400^{th} hysteresis loops are presented, along with predictions of stress range ($\Delta\sigma = |\max(\sigma_i)| + |\min(\sigma_i)|$, for the i^{th} loading cycle) evolution over the 400 cycle range. Similar plots are presented in figure 14 (by way of validation) for in phase an-isothermal $400^oC - 500^oC$ conditions, also for a 400 cycle test range. Two additional an-isothermal experimental results were available at the time of writing ($400^oC - 600^oC$ in phase and $400^oC - 600^oC$ out of phase) however in both cases these were limited to 8 cycles worth of data. Failure of experimental control systems led to the premature conclusion of the $400^oC - 600^oC$ in phase and $400^oC - 600^oC$ out of phase experiments, however the authors have decided to present

here what data could be extracted from the results in order to further compare the model predictions to (albeit limited) experimental data. Predictions of both of these conditions, for the 1^{st}, 4^{th}, and 8^{th} cycles, are presented in figures 15 and 16, respectively. Readers should note that, in lower temperature stress range ($\Delta\sigma$) plots (figure 12 d). for example), some apparent cyclic hardening can be observed. In actuality, this is a result of the way in which $\Delta\sigma$ is calculated on a cycle by cycle basis. For the first cycle, maximum stresses relate to the peak stresses after monotonic (quarter cycle) loading (see figure 12 a). for an example of this). As such, viscous stresses have not accumulated to the same degree as they would have during a full half cycle. In situations where viscous stress can accumulate more quickly (i.e. at higher temperatures), this effect is less obvious, and these effects are of course not observed at all in full hysteresis loop data.

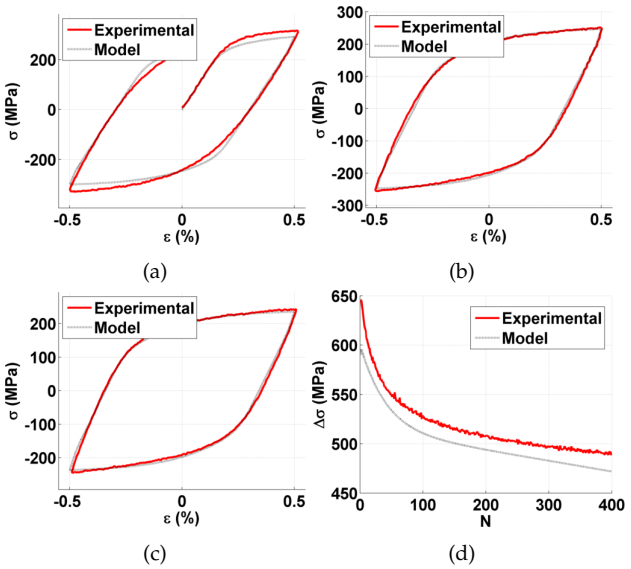

Figure 9: A comparison between experimental and predicted (using the functions given in equation (21)) stress response (a-c, cycles 1, 200 and 400, respectively) and stress range (d) for P91 under isothermal (600^oC) conditions and "saw tooth" type ($R = -1, \pm 0.5\%$) loading conditions.

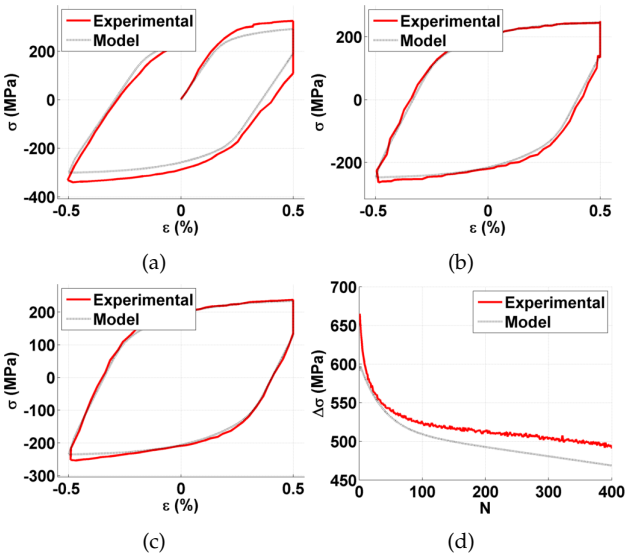

Figure 8: A comparison between experimental and predicted (using the functions given in equation (21)) stress response (a-c, cycles 1, 200 and 400, respectively) and stress range (d) for P91 under isothermal (600^oC) conditions and "dwell" type ($R = -1, \pm 0.5\%$) loading conditions.

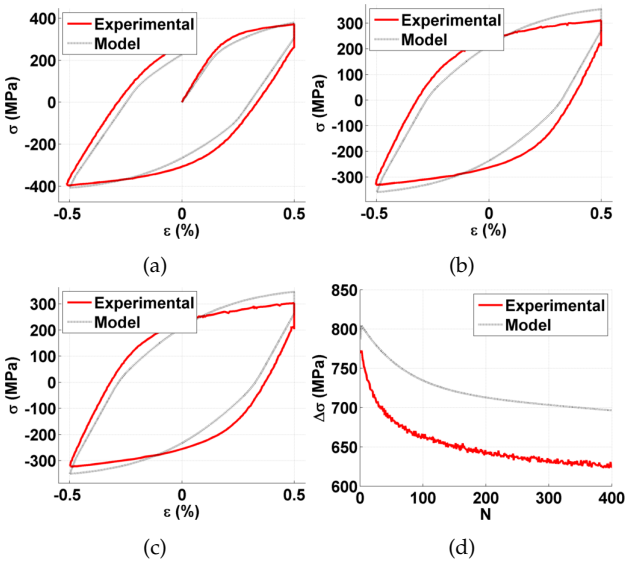

Figure 10: A comparison between experimental and predicted (using the functions given in equation (21)) stress response (a-c, cycles 1, 200 and 400, respectively) and stress range (d) for P91 under isothermal (500^oC) conditions and "dwell" type ($R = -1, \pm 0.5\%$) loading conditions.

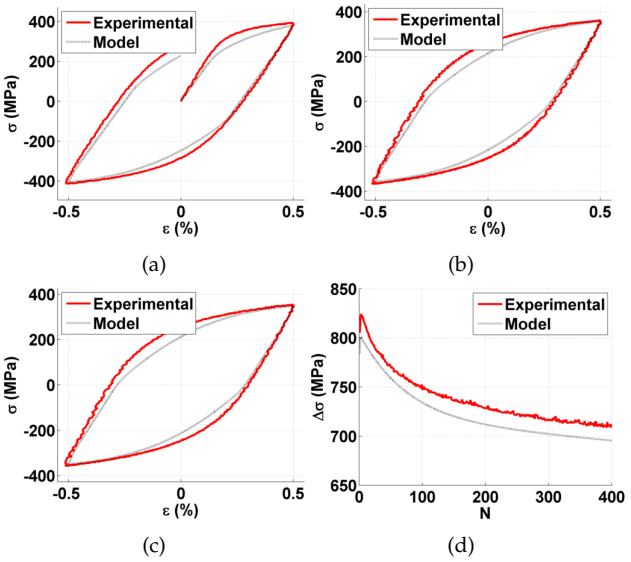

Figure 11: A comparison between experimental and predicted (using the functions given in equation (21)) stress response (a-c, cycles 1, 200 and 400, respectively) and stress range (d) for P91 under isothermal (500^oC) conditions and "saw tooth" type ($R = -1$, $\pm 0.5\%$) loading conditions.

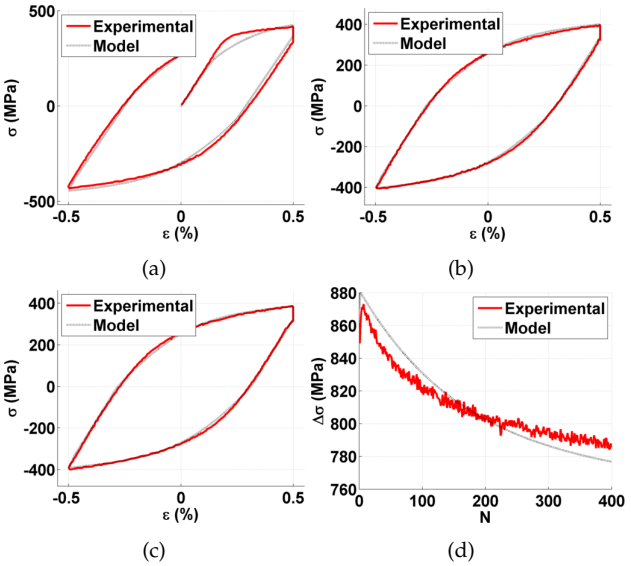

Figure 12: A comparison between experimental and predicted (using the functions given in equation (21)) stress response (a-c, cycles 1, 200 and 400, respectively) and stress range (d) for P91 under isothermal (400^oC) conditions and "dwell" type ($R = -1$, $\pm 0.5\%$) loading conditions.

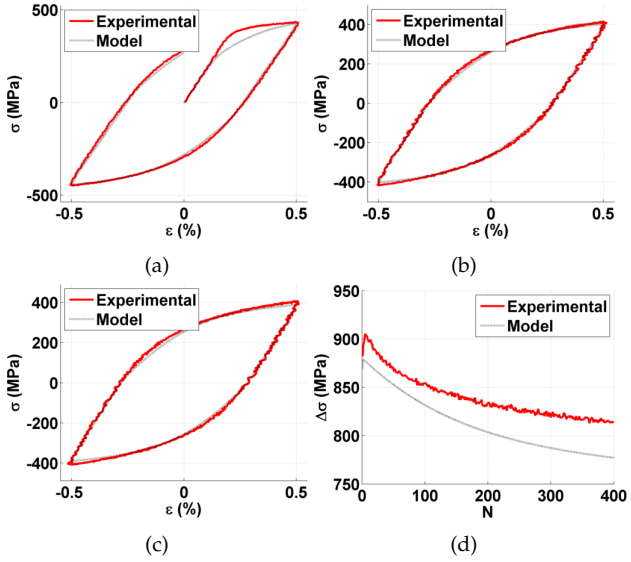

Figure 13: A comparison between experimental and predicted (using the functions given in equation (21)) stress response (a-c, cycles 1, 200 and 400, respectively) and stress range (d) for P91 under isothermal (400^oC) conditions and "saw tooth" type ($R = -1$, $\pm 0.5\%$) loading conditions.

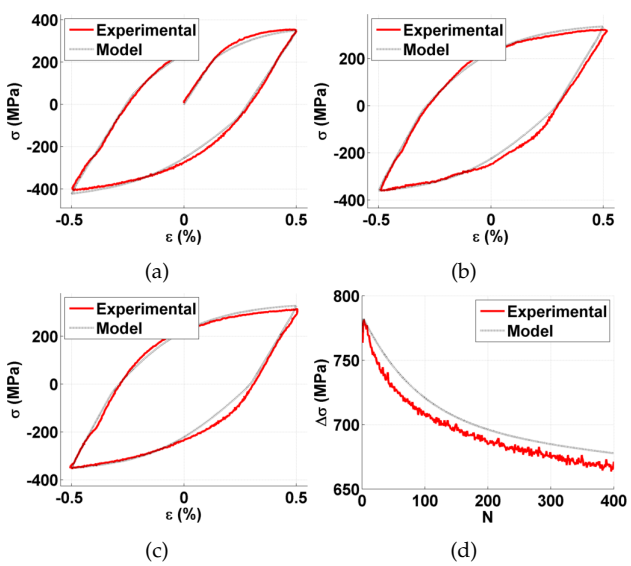

Figure 14: A comparison between experimental and predicted (using the functions given in equation (21)) stress response (a-c, cycles 1, 200 and 400, respectively) and stress range (d) for P91 under an-isothermal in phase ($400 - 500^oC$, $R = -1$, $\pm 0.5\%$) conditions.

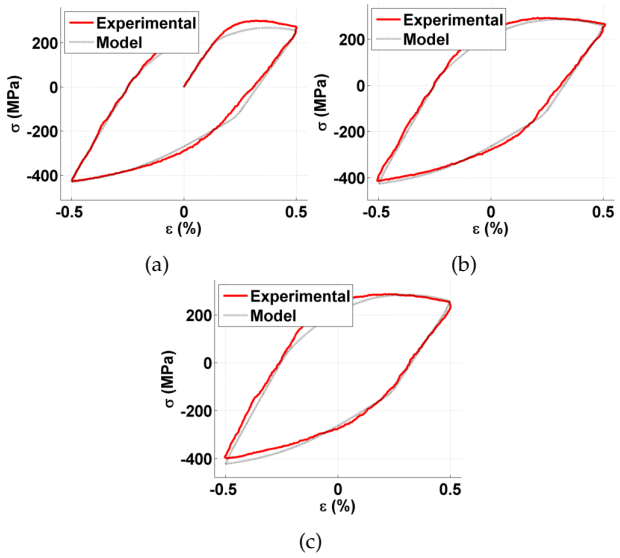

Figure 15: A comparison between experimental and predicted (using the functions given in equation (21)) stress response (a-c, cycles 1, 4 and 8, respectively) for P91 under an-isothermal in phase ($400 - 600^oC$, $R = -1$, $\pm 0.5\%$) conditions.

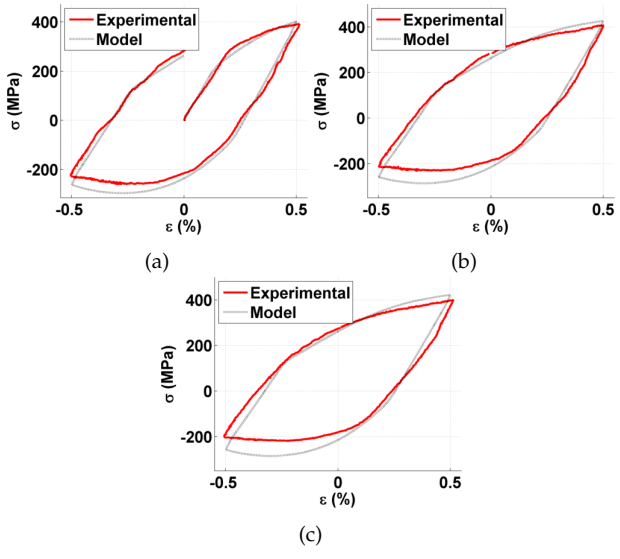

Figure 16: A comparison between experimental and predicted (using the functions given in equation (21)) stress response (a-c, cycles 1, 4 and 8, respectively) for P91 under an-isothermal out of phase ($400 - 600^oC$, $R = -1$, $\pm 0.5\%$) conditions.

3.4 Thermal and Mechanical FEA Models

In decoupled thermal-mechanical analyses, temperature fields are initially found by solving the heat equation for the component to be analysed. Time dependent temperature fields may be applied to mechanical models so that point wise thermal strains and temperature dependent material properties can be evaluated. In the present work, thermal and mechanical analyses were solved using ABAQUS, utilising DC3D10 and C3D10 elements, respectively[24]. As discussed in the introduction to the present work, heat transfer coefficients are either varying or uniform (constant) fields and are determined from CFD analyses (see section 2). Heat transfer coefficient fields where applied to the model on a node basis using ABAQUS's FILM user subroutine feature[24], with nodal coefficient values mapped from the CFD mesh using interpolation functions within MATLAB . Thermal material constants have been taken from the work of Yaghi *et al.*[30] (table 4). A negligible dependency is assumed in density (ρ) and Poisson's ratio (ν) over the tested temperature range. As such, values for these quantities are taken to be $7.76 \times 10^3 kg/m^3$ and 0.3, respectively. The assumption of temperature independent Poisson's ratio that is used here is taken from the work of Yaghi et al.[30] and Barrett et al.[6], however readers should note that slight temperature dependencies do exist. At present, there is little published experimental data to quantify these dependencies however this should be a focus for the community in the future, particularly for industry relevant materials such as P91. .

An overview of the mechanical FEA models is presented in figure 17. Internal pressure loads (which were assumed to be in phase with the temperature loads shown in figure 2) were applied over the internal shell and stud penetration surfaces, with proportional pressures applied to end faces on the same regions in order to satisfy closed end conditions. Symmetry was enforced in the YZ plane ($\theta = 0, \pi$ in figures 5 and 6) by setting displacements in the X direction (u_X) to zero. Unit cell end conditions were enforced by setting Z displacements (u_Z) to zero at one end and by applying an equation type constraint[24] at the other (thereby ensuring planar motion). Temperature fields were of course imported from the appropriate thermal analysis as a pre-defined field.

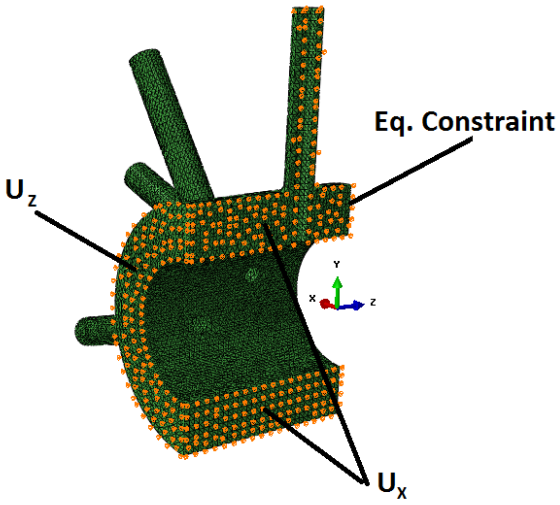

Figure 17: Boundary conditions used in mechanical FEA models.

Table 4: A summary of the temperature-dependent material constants (representative of a P91 chromium steel), taken from the work of Yaghi *et al.*[30], used in the FEA thermal models.

Temperature (°C)	Thermal Conductivity (k) ($W/m.K$)	Specific Heat Capacity (C_P) ($kJ/kg.K$)
200	28	0.51
250	28	0.53
300	28	0.55
350	29	0.57
375	29	0.585
400	29	0.6
450	29	0.63
500	30	0.66
550	30	0.71
600	30	0.77
650	30	0.86
700	30.5	0.942

3.5 Results

Accumulated plastic strain (p) levels are presented here as scalar metrics which may be used to judge analyses performed with varying and uniform heat transfer coefficient fields (p is a useful parameter to consider as many damage qualities are at least in part dependent upon it[17]). An example contour plot showing p is presented in figure 18. Generally speaking peak plastic strains are observed at the inner bore saddles[2], therefore two sampling points (A and B) have been defined over the saddle for the central stub penetration (see figure 18).

The accumulation of p at these points over the duration of the simulations is plotted in figures 19 to 22 for the various loading/boundary conditions. For clarity, figures 19 to 22 show results for a $2.5hr$ start (using full load thermal BCs, see figure 5), a $0.5hr$ start (using full load thermal BCs), and two $0.25hr$ starts (using full load thermal BCs and half load thermal BCs, see figure 6), respectively. Readers should note that the results presented in figures 19 to 22 are for a single loading cycle, as presented in figure 2. As such, increments in p tend to zero at the end of the loading cycle as the material elements move from a high temperature/highly stressed state (at the end of the generation hold period) to a low temperature/moderately stressed state at the end of the loading cycle. In this final state the material response predicted by the elastic visco-plastic model is elastic.

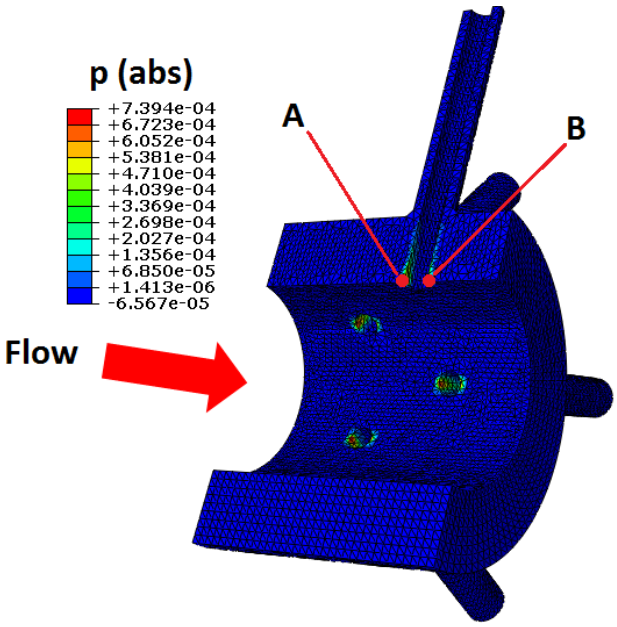

Figure 18: Example FEA results (showing accumulated plastic strain p) and the locations of the component sampling points A and B.

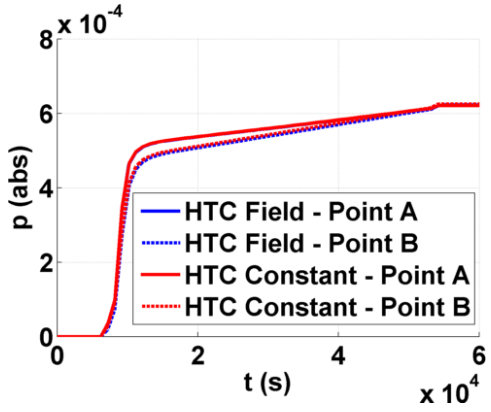

Figure 19: Plastic strain accumulation for uniform and varying shell heat transfer coefficient fields, assuming full load flow conditions and a 2.5*hr* start.

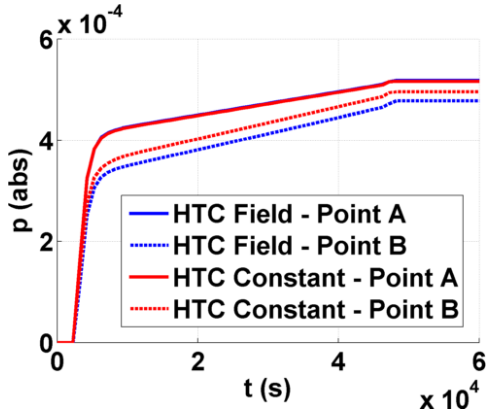

Figure 20: Plastic strain accumulation for uniform and varying shell heat transfer coefficient fields, assuming full load flow conditions and a 0.5*hr* start.

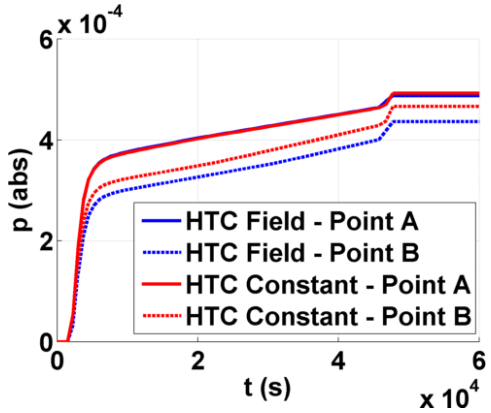

Figure 21: Plastic strain accumulation for uniform and varying shell heat transfer coefficient fields, assuming full load flow conditions and a 0.25*hr* start.

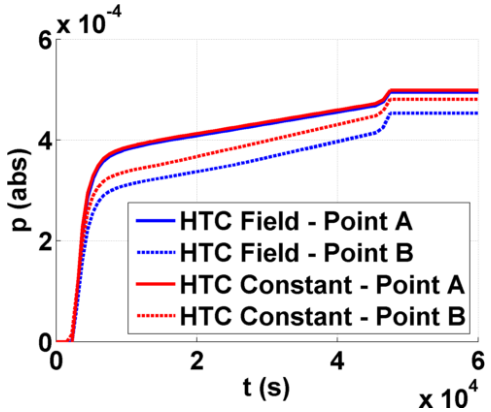

Figure 22: Plastic strain accumulation for uniform and varying shell heat transfer coefficient fields, assuming half load flow conditions and a 0.25*hr* start.

4 Conclusions and Future Work

A CFD study of a superheater outlet steam header has been conducted in order to estimate local heat transfer coefficients for typical plant load conditions, assuming full and partial load steam flow rates. These thermal boundary conditions have been used to determine transient temperature fields and consequently thermally dependent mechanical component response. Comparisons have been made between commonly accepted thermal boundary conditions and the more refined CFD based approximations. While the header component considered here is taken from a coal power plant, similar examples (also made from P91) may be found in combined cycle gas turbine (CCGT) plant. Observations discussed here are therefore directly transferable.

In all cases, there is a good level of agreement between sampling point A results (i.e they appear to be independent of the particular thermal boundary conditions applied). Such results are to be expected as heat transfer coefficient "cool spots" are observed ahead of the stub penetrations (i.e. in the wake of the upstream row of stubs, see figures 5 and 6). Local heat transfer coefficient fields are therefore approximately identical for the two thermal boundary condition approaches (variable and uniform field). These locations are the sites of peak plastic strain increments during loading, therefore the presented results suggest a life limiting approximation of the header can be readily achieved using CFD average results. Future studies in this area can justifiably avoid a great deal of complexity by using uniform heat transfer coefficient fields. Care must however be taken when attempting to approximate inter-ligament cracking, such appropriate values for the heat transfer coefficient chosen to reflect the different flow patterns stud and shell sections of the header component. Using the above recommendations, almost identical mechanical behaviours may be observed for the two heat transfer coefficient definition methods, meaning that even sophisticated crack initiation methods, such as the memory surface concept pro-

posed by Jiang[31] for multi-axial problems, will yield almost identical results.

The mechanical response predicted by the two heat transfer coefficient definition methods is compared in figure 23. Stress and strain components have been extracted from FEA simulations at analysis point B for the full load, $0.25hr$ start conditions (see figure 21). This condition was selected as it induced the greatest difference in plastic strain accumulation profiles. Hoop stress and strain are considered here as the hoop direction at analysis point B aligns well with the maximum principal direction. Industrial evidence of inter-ligament cracking over the stub saddles also suggests that loading in this direction is critical for understanding crack initiation and propagation. In the current context, perhaps the most important observation that can be made from these plots is that the largest difference between the two methods occurs during ramp up, when compressive stresses are induced in the material element around analysis point B. Such effects are to be expected in both heat transfer coefficient definitions as, at this point in the operational history, large thermal gradients exist at locations such as analysis point B. The "cool spot" behind stub penetrations (flanked by two "warm spots", see figure 5) compresses this location that would otherwise be in tension. It is only when the local temperature variations that exist in these regions have dissipated that tensile stress states (due to the internal steam pressure) can be observed (which are almost identical for both cases, see figure 23 b).). Similar features can be seen towards the end of the loading cycle, where compressive stress states are again achieved due to the local thermal gradients and low internal pressures.

Some degree of asymmetry between points A and B is to be expected due to the particular boundary conditions applied to the structure. This source of asymmetry is not the focus of the present work, rather we are concerned here with the additional asymmetry observed as a result of applying a variable field of heat transfer coefficients. The heat transfer coefficient "hot spots" that can be observed in the wake of the stub penetrations reduce local temperature gradients, thereby limiting local thermal strain components and (consequently) accumulated plasticity. The thermal diffusivity of P91 can be approximated to $5.021x1-^{-6}\,m^2/s$ and, assuming a characteristic length equal to the thickness of the shell region ($89mm$), a characteristic time for the header component of $0.438hrs$ can be found. When a start is on the same order of this characteristic time local thermal gradients will be more pronounced in the shell through thickness direction. Therefore, a greater difference between asymptotic point A and B results is to be expected for shorter start times. This effect is only exaggerated by the wake heat transfer coefficient field, acting to increase the difference between point B p levels (see table 5).

Table 5: A summary of percentage differences in p (between differing thermal boundary conditions) at sampling point B for various loading patterns.

Load Pattern and Thermal BC	% Difference
Full Load Flow, 2.5hr Start	0.52
Full Load Flow, 0.5hr Start	3.53
Full Load Flow, 0.25hr Start	6.47
Half Load Flow, 0.25hr Start	5.78

A level of conservatism in header component visco-plastic behaviour prediction has been identified in the present work, stemming from the application of simplified thermal boundary conditions. This is likely to be of little industrial interest as life limiting behaviours are still predicted well using the simplified thermal boundary conditions. Several areas of possible future development exist however that may highlight cases where the additional CFD effort is warranted. Of particular interest is the modelling of features which induce more complex flow fields, such as the main steam pipe outlet. Such work is likely to require new unit cells, or, preferably, full CFD models of the header component. Furthermore, the validity of decoupled solutions should be tested against fully coupled CFD-thermal-mechanical solutions. Once the effects of variable heat transfer coefficient boundary conditions have been determined for an idealised component (using either coupled or decoupled analysis techniques) more realistic discontinuities, such as weldment material boundaries and variations in the component geometry resulting from manufacture or service exposure, may be incorporated and investigated.

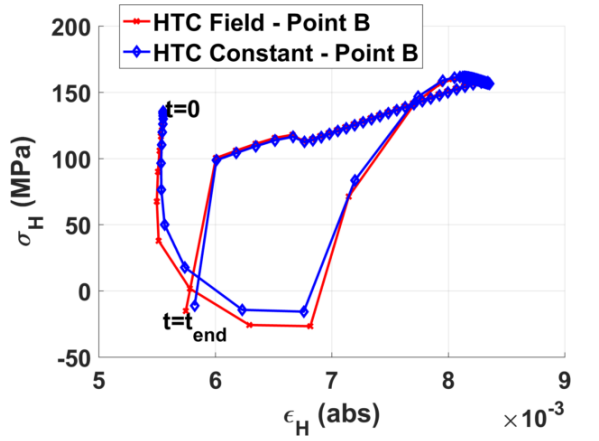

(a)

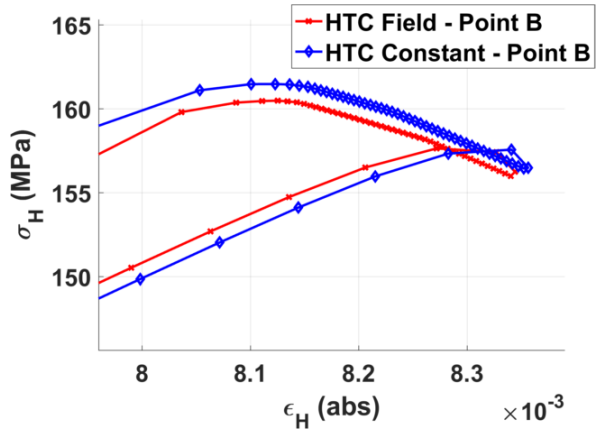

(b)

Figure 23: A comparison of hoop stress/hoop strain (σ_H and ϵ_H, respectively) hysteresis loops (for a single loading cycle) for analysis point B (see figure 18). The results presented here are extracted from FEA simulations which assume full load flow conditions and a $0.25hr$ start (a plot of plastic strain accumulation, p, for this case can seen in figure 21). Full hysteresis loops for the two heat transfer coefficient definition methods may be seen in a)., with a close up of peak stress and strain conditions in b). Note that, in the above figures, t_{end} indicates the time at the end of loading cycle.

A brief discussion was made in section 2.1 on the choice of steam properties (defined by the chosen conditions, operating temperature and pressure, see table 1) that were implemented in CFD simulations in order to estimate the heat transfer coefficient fields that were used in the present work. Full load ($841K$ and $166bar$) conditions were chosen so that the steam flow considered was most representative of the point in operation when the header material experiences its lowest strength state and corresponding viscous effects are most significant. In order to investigate the effect that the choice of steam properties has on heat transfer coefficient field, addition CFD simulations have been performed using alternative steam conditions. These conditions are representative of partial load (i.e. the load at which a generation unit may be held such that it can return to full load quickly should the market demand it), namely 420^oC $(693K)$ and $99bar$. Profiles of heat transfer coefficient (based on full and partial load steam conditions) are presented in figure 24 b)., with the location of sampling defined in figure 24 a). Note that, in figure 24 b)., spatial positions around the circumference of the header shell are normalised, with the 0 position relating the to central stub location in figure 24 a). Of notable interest in figure 24 are the significantly higher spatial gradients in heat transfer coefficient values observed for the partial load (420^oC) case, which are approximately 3-4 times greater the those observed in the full load (568^oC) case (note that the full load conditions were used in the majority of the work presented in the current paper). These spatial gradients result from the wake flow patterns which form behind the header stub penetrations (see figures 5 and 6), and are the reason for high thermal gradients (and consequently thermal strain) at the points of interest identified in figure 19. It is unclear at present how theses higher thermal gradients will affect the results presented here, particularly when we recall that the conditions under which they arise are at a lower temperature and therefore less arduous for the material in the first instance. The effects highlighted in figure 24 do indicate the complicated nature of the heat transfer coefficient field and emphasise that it is a dynamic quantity. Future work must quantify the effect that the variable heat transfer coefficient field has on stress analysis, either by considering heat transfer coefficient fields resulting from multiple industry relevant steam conditions or by conducting more sophisticated coupled CFD/FEA simulations, wherein temporal and spatial distributions in heat transfer coefficient are incorporated into the analyses.

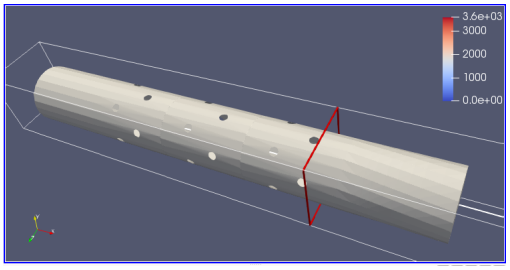

(a)

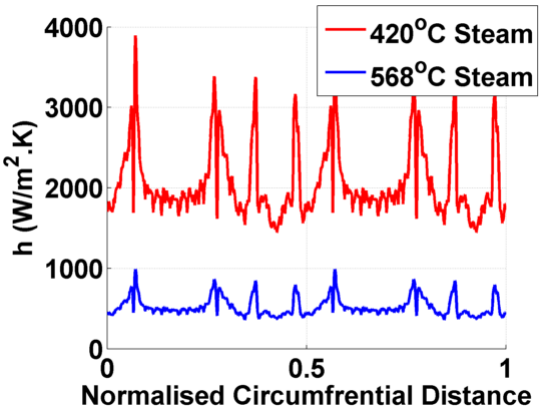

(b)

Figure 24: A comparison of heat transfer coefficient profiles, extracted from CFD analyses downstream of the stub penetrations, showing a). the location of the sampling and b). the results for the full load 568^oC ($841K$ and $166bar$) and partial load 420^oC ($693K$ and $99bar$) conditions.

5 Acknowledgements

The authors acknowledge the computational resources provided by HPC Midlands Plus.

References

[1] Beatt RJI, Birch WL, Hinton SE, Kelly M, Pully MJ, Wright GRL, et al. Two-Shift Operation of 500 MW Boiler/Turbine Generating Units. Proceedings of the Institution of Mechanical Engineers, Part A: Journal of Power and Energy. 1983;197:247–255.

[2] Farragher TP, Scully S, O'Dowd NP, Leen SB. Development of Life Assessment Procedures for Power Plant Headers Operated Under Flexible Loading Scenarios. International Journal of Fatigue. 2013;49:50–61.

[3] Rouse JP, Hyde CJ. A Comparison of Simple Methods to Incorporate Material Temperature Dependency in the Green's Function Method for Estimating Transient Thermal Stresses in Thick-Walled Power Plant Components. Materials. 2016;9:26.

[4] Kumar R, Sharma AK, Tewari PC. Thermal Performance and Economic Analysis of 210 MWe Coal-Fired Power Plant. Journal of Thermodynamics. 2014;2014:520183.

[5] Gostling J. Two Shifting of Power Plant: Damage to Power Plant Due to Cycling - A Brief Overview. Operation Maintenance and Materials Issues. 2002;1:1–9.

[6] Barrett RA, O'Donoghue PE, Leen SB. An Improved Unified Viscoplastic Constitutive Model for Strain-Rate Sensetivity in High Temperature Fatigue. International Journal of Fatigue. 2013;48:192–204.

[7] Rouse JP, Hyde CJ, Sun W, Hyde TH. Comparison of Several Optimisation Strategies for the Determination of Material Constants in the Chaboche Visco-Plasticity Model. Journal of Strain Analysis in Engineering Design. 2013;Revision Submitted.

[8] Saber M, Sun W, Hyde TH. Numerical study of the effects of crack location on creep crack growth in weldment. Engineering Fracture Mechanics. 2016;154:72–82.

[9] Viswanathan R. Damage Mechanisms and Life Assessment of High Temperature Components. ASM International; 1989.

[10] Viswanathan R, Stringer J. Failure Mechanisms of High Temperature Components in Power Plants. Journal of Engineering Materials and Technology. 2000;122:246–255.

[11] Menter FR. Two-Equation Eddy-Viscosity Turbulence Models for Engineering Applications. AIAA Journal. 1994;32:1598–1605.

[12] Rogers GFC, Mayhew YR. Thermodynamic and Transport Properties of Fluids. 5th ed. Blackwell; 1995.

[13] Chaboche JL, Rousselier G. On the Plastic and Viscoplastic Constitutive-Equations - Part 1: Rules Developed with Internal Variable Concept. Journal of Pressure Vessel Technology - Transactions of the ASME. 1983;105:153–158.

[14] Chaboche JL, Rousselier G. On the Plastic and Viscoplastic Constitutive-Equations - Part 2: Application of Internal Variable Concepts to the 316 Stainless-Steel. Journal of Pressure Vessel Technology - Transactions of the ASME. 1983;105:159–164.

[15] Kyaw ST, Rouse JP, Lu J, Sun W. Determination of Material Parameters for a Unified Viscoplasticity-Damage Model for a P91 Power Plant Steel. International Journal of Mechanical Sciences. 2016;115-116:168–179.

[16] Tong J, Vermeulen B. The Description of Cyclic Plasticity and Viscoplasticity of Waspaloy Using Unified Constitutive Equations. International Journal of Fatigue. 2003;25:413–420.

[17] Lemaitre J, Chaboche JL. Mechanics of Solid Materials. Cambridge; 2000.

[18] Boresi AP, Chong KP, Lee JD. Elasticity in Engineering Mechanics. Wiley; 2011.

[19] Chaboche JL. A Review of some Plasticity and Viscoplasticity Constitutive Theories. International Journal of Plasticity. 2008;24:1642–1693.

[20] Zhan ZL, Tong J. A Study of Cyclic Plasticity and Viscoplasticity in a New Nickel-Based Superalloy Using Unified Constitutive Equations. - Part 1: Evaluation and Determination of Material Parameters. Mechanics of Materials. 2007;39:64–72.

[21] Zhan ZL, Tong J. A Study of Cyclic Plasticity and Viscoplasticity in a New Nickel-Based Superalloy Using Unified Constitutive Equations - Part 2: Simulation of Cyclic Stress Relaxation. Mechanics of Materials. 2007;39:73–80.

[22] Zhang Z, Delagnes D, Bernhart G. Anisothermal Cyclic Plasticity Modeling of Martensitic Steels. International Journal of Fatigue. 2002;24:635–648.

[23] Chaboche JL. Time-Independent Constitutive Theories for Cyclic Plasticity. International Journal of Plasticity. 1986;2:149–188.

[24] ABAQUS 2016 Online Documentation. Dassault Syste'mes; 2016.

[25] Dunne F, Petrinic N. Introduction to Computational Plasticity. Oxford University Press; 2011.

[26] Cottrell AH. Dislocations and Plastic Flow in Crystals. 1st ed. Oxford, U.K.: Oxford University Press; 1953.

[27] Fournier B, Sauzay M, Caes C, Noblecourt M, Mottot M. Analysis of the Hysteresis Loops of a Martensitic Steel: Part I: Study of the Influence of Strain Amplitude and Temperature under Pure Fatigue Loadings using an Enhanced Stress Partitioning Method. Materials Science and Engineering: A. 2006;437:183–196.

[28] Optimisation Toolbox TM 4 User's Guide. T. M. Inc; 2008.

[29] MATLAB 7 Mathematics. T. M. Inc; 2008.

[30] Yaghi A, Hyde TH, Becker AA, Williams JA, Sun W. Residual Stress Simulation in P91 Pipe Welds. Journal of Materials Processing Technology. 2005;167:480–487.

[31] Jiang Y. A fatigue criterion for general multiaxial loading. Fatigue & Fracture of Engineering Materials & Structures. 2000;23:19–32.